



Optics Letters

Scalable terahertz generation by large-area optical rectification at 80 TW laser power

DOGEUN JANG,¹ CHUL KANG,^{2,4} SEONG KU LEE,^{2,3} JAE HEE SUNG,^{2,3} CHUL-SIK KEE,² SEUNG WOO KANG,^{2,3} AND KI-YONG KIM^{1,5}

¹Institute for Research in Electronics and Applied Physics, University of Maryland, College Park, Maryland 20742, USA

²Advanced Photonics Research Institute, Gwangju Institute of Science and Technology, 123 Cheomdangwagi-ro, Oryong-dong, Buk-gu, Gwangju, 61005, South Korea

³Center for Relativistic Laser Science, Institute for Basic Science, 123 Cheomdangwagi-ro, Buk-gu, Gwangju, 61005, South Korea

⁴e-mail: iron74@gjst.ac.kr

⁵e-mail: kykim@umd.edu

Received 17 July 2019; revised 12 September 2019; accepted 15 October 2019; posted 28 October 2019 (Doc. ID 372730); published 14 November 2019

We demonstrate high-energy terahertz generation from a large-aperture (75-mm diameter) lithium niobate wafer by using a femtosecond laser with energy up to 2 J. This scheme utilizes optical rectification in a bulk lithium niobate crystal, where most terahertz energy is emitted from a thin layer of the rear surface. Despite its simple setup, this scheme can yield 0.19 mJ of terahertz energy with laser-to-terahertz conversion efficiencies of $\sim 10^{-4}$, about 3 times better than ZnTe when pumped at 800 nm. The experimental setup is upscalable for multimillijoule terahertz generation with petawatt laser pumping. © 2019 Optical Society of America

<https://doi.org/10.1364/OL.44.005634>

Provided under the terms of the OSA [Open Access Publishing Agreement](#)

High-power terahertz generation is of great interest for its own study and potential applications in nonlinear terahertz spectroscopy and imaging, as well as exploration of terahertz driven extreme nonlinearities [1–4]. Optical rectification (OR) is widely used to produce single-cycle broadband terahertz radiation with femtosecond laser pulses. In general, OR is well suited for scalable terahertz generation—one can simply increase the OR crystal surface area with more input laser energy. Previously, a large-diameter (75 mm) ZnTe was used to produce 1.5 μJ of terahertz radiation with conversion efficiency of 3.1×10^{-5} [5]. However, two-photon absorption in ZnTe with 800 nm pumping results in laser energy depletion and terahertz screening by charge carrier generation, fundamentally limiting maximum useable laser intensities on the crystal surface. One method to overcome the limitation is using a longer-wavelength pump laser to suppress two-photon absorption in ZnTe [6,7].

Organic crystals are also commonly used for high-energy terahertz generation due to their extremely high nonlinearities [8,9]. However, organic crystals have low damage thresholds with large optical and terahertz absorption [8]. Generally, they

are not favorable for optical pumping at 800 nm, and the growth of large-size organic crystals is also challenging. Nonetheless, monolithic arrays of partitioned organic crystals have been used to generate 0.9 mJ of terahertz radiation with 1,250 nm pumping [9].

Lithium niobate (LN) is another strong candidate for scalable terahertz generation because of its high nonlinearities and damage thresholds [10]. Owing to its large bandgap (~ 4 eV), LN is free from two-photon absorption at 800 nm. Moreover, high-quality, large-size LN wafers are commercially available with diameters beyond 152 mm. For efficient phase matching at 800 nm, a tilted pulse front method is routinely used for high-energy terahertz generation [11–16]. Recently, terahertz energy of 0.2 mJ was produced from a 68 mm \times 68 mm \times 64 mm sized LN prism with laser energy up to 70 mJ [16]. The prism-based geometry, however, induces nonuniform pump interaction due to its large tilt angle of 63° necessary for excitation at 800 nm. This results in poor terahertz beam quality [17,18]. The condition can be even worse with large input beam sizes, which limits its potential use with multijoule laser pumping.

In this Letter, we examine scalable terahertz generation from LN in the form of a large-area wafer. Planar LN crystals are frequently used as OR materials, but their terahertz conversion efficiencies are not well known especially under extremely high laser energy and intensity conditions. Here we study laser chirp dependent terahertz generation and determine the ultimate terahertz conversion efficiency in LN wafers at 800 nm excitation.

A schematic of our experimental setup is shown in Fig. 1(a). In this experiment, a 150 TW Ti:sapphire laser capable of producing 25 fs, 4 J pulses at a repetition rate of 5 Hz is used. Owing to possible cumulative degradation of the compressor gratings, the laser is operated in a single-shot mode. The laser pulse is p-polarized and clipped by an iris diaphragm to reduce the beam diameter to 50 mm with a maximum laser energy of 2 J after the iris. The laser spectrum is centered at 807 nm with a 60 nm bandwidth in full width at half-maximum (FWHM)

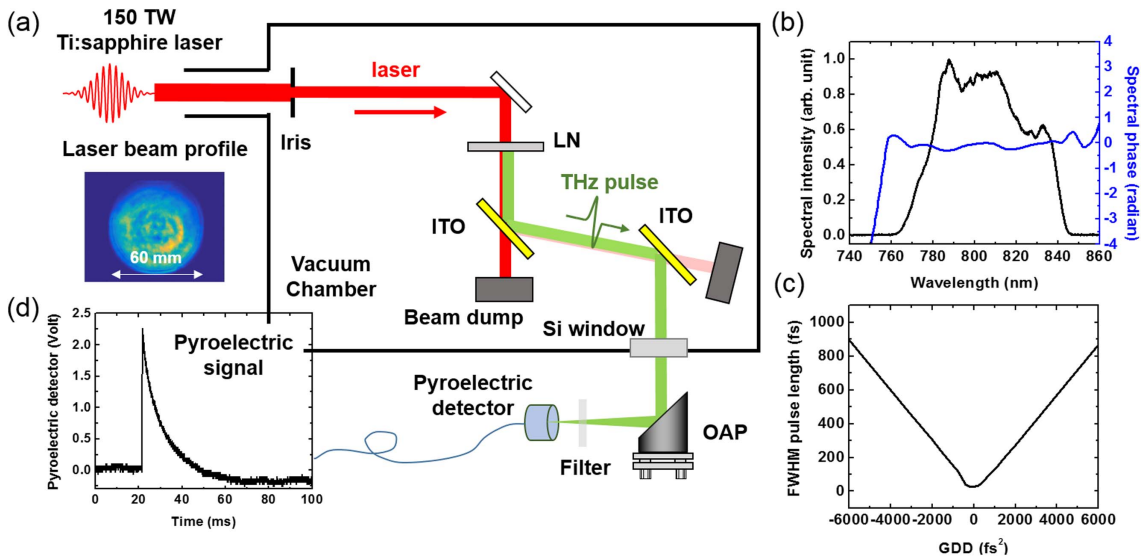


Fig. 1. (a) Experimental setup for high-energy terahertz generation from a large-aperture LN wafer. The inset shows the incident laser beam profile. (b) Laser spectral power (black line) and spectral phase (blue line). (c) Estimated laser pulse duration as a function of laser GDD. (d) Sample pyroelectric detector signal.

as shown in Fig. 1(b). The laser pulse duration is adjusted by adding group delay dispersion (GDD), either positive or negative, with an acousto-optic programmable dispersive filter in the laser system. This provides a pulse width range of 25–900 fs [see Fig. 1(c)]. Three types of congruent LN are examined for terahertz generation—x-cut (0.5-mm-thick and 1.0-mm-thick) and y-cut (0.5-mm-thick) wafers, all with a 75-mm diameter. In the setup, the LN wafer is aligned with its extraordinary z axis parallel to the laser p-polarization direction for maximal terahertz generation. This configuration yields p-polarized terahertz emission. To decouple the resulting terahertz radiation from its copropagating laser pulse, two optical windows coated with 250-nm-thick tin-doped indium oxide (ITO) layers are used to reflect the terahertz radiation. To minimize reflection at 800 nm, the ITO-coated windows are tilted at Brewster’s angle of 56°. This yields 800 nm and 1 THz reflection of 0.1% and 88%, respectively. Double reflection with two parallel ITO windows provides overall terahertz reflection of 77%, with <0.0001% reflection at 800 nm. The reflected terahertz pulse is brought into air through a 10-mm-thick, high-resistivity Si window that transmits ~50% of terahertz energy but

completely blocks the attenuated laser pulse. The maximum laser fluence on the Si surface is 0.1 $\mu\text{J}/\text{cm}^2$, sufficiently low enough to avoid potential charge carrier generation and subsequent terahertz screening.

The transmitted terahertz pulse is focused by a metallic, 90° off-axis parabolic (OAP) mirror with 102-mm-diameter and 152-mm focal length. The terahertz energy is measured with a pyroelectric detector (Gentec, THz5D-MT-BNC) with filters including one or more calibrated terahertz attenuators (Tydex, ATS-5-50.8), a 1.0-mm-thick Si filter, and a lowpass terahertz filter (Tydex, LPF-10.9-47) providing a cutoff frequency of 10 THz. The responsivity of the detector is measured at 800 nm with 0.9 $\mu\text{J}/\text{V}$ in a single-shot mode [see Fig. 1(d)] and converted to 1.8 $\mu\text{J}/\text{V}$ at <3 THz frequencies by using calibration data provided by Gentec. First, LN crystal-cut and laser chirp dependence are studied. Figure 2 shows terahertz output energy as a function of laser GDD for the three types of LN. In general, at laser energy below 0.6 J, the shorter pulse duration yields the higher terahertz energy. However, at laser energy equal to or greater than 1.2 J, the short pulse condition exhibits suppressed terahertz signals, with a bit longer pulse

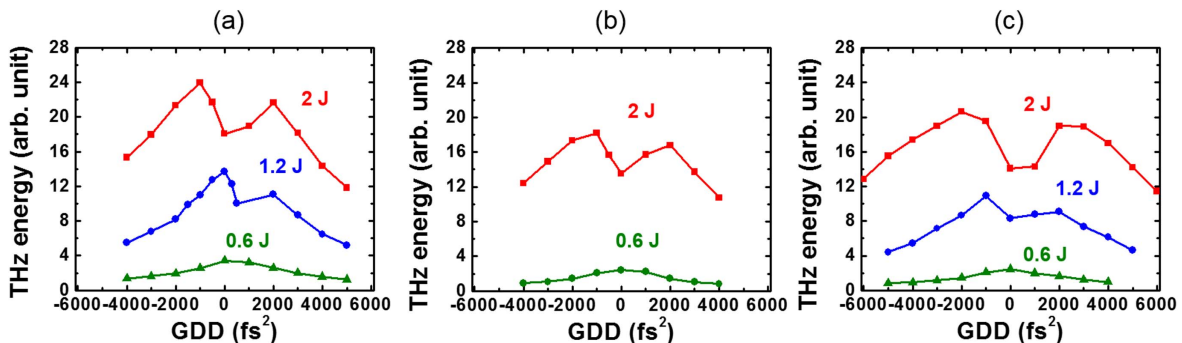


Fig. 2. Terahertz output energy as a function of laser GDD with 0.6 J (green triangles), 1.2 J (blue circles), and 2 J (red squares) energy incident on a LN wafer of (a) x-cut and 0.5 mm thickness, (b) y-cut and 0.5 mm thickness, and (c) x-cut and 1 mm thickness.

width conditions (100–200 fs) yielding more terahertz radiation. This is due to laser energy depletion via three-photon absorption in LN occurring at high laser intensities. Note that three laser photons (1.5 eV each) can be simultaneously absorbed to exceed the bandgap of LN (~ 4 eV) and produce charge carriers. A similar behavior was previously observed with a tilted pulse front scheme using a thick LN prism [15,16]. Also, for the same pulse duration, the negatively chirped ones, in general, yield slightly higher terahertz energy compared to the positive ones. This is due to dispersion in LN—a negatively chirped laser pulse undergoes temporal compression, producing higher laser intensity for terahertz generation, in contrast to a positively chirped one experiencing pulse stretching. In addition, an asymmetric laser chirp with high-order dispersion present in the laser system [see Figs. 1(b) and 1(c)] is also responsible for the observed GDD dependence.

Figure 3(a) shows terahertz versus laser energy scaling for the three LNs. The y axis represents terahertz energy estimated right after the LN crystal. Here the GDD value is fixed at $-1,000$ fs² for the 0.5-mm-thick wafers and $-2,000$ fs² for the 1.0-mm-thick LN. In general, the terahertz output energy continuously increases with input laser energy, also exhibiting saturation behaviors with high laser energy (>1.8 J). The corresponding laser-to-terahertz conversion efficiency is shown in Fig. 3(b). With the x-cut, 0.5-mm-thick LN, the maximum terahertz energy produced is ~ 180 μ J with the conversion efficiency approaching 10^{-4} .

The radiation spectrum is characterized with five sets of metal-mesh bandpass filters (Thorlabs) [18] and shown in Fig. 3(c). All filters are calibrated, and their spectral transmission curves are plotted in Fig. 3(c). Here the terahertz spectrum (circles) is obtained by dividing the detected pyroelectric signal by the product of the width (FWHM) and height of each filter's transmission curve [19]. The resulting spectrum peaks at 1 THz and falls with increasing terahertz frequency.

To simulate terahertz generation in a bulk LN, we solve one-dimensional (1D) coupled forward Maxwell equations (FME) given by

$$\frac{\partial E_T}{\partial \zeta} = -\left(\frac{\alpha}{2} + iD_T\right)E_T - i\frac{2d_{\text{eff}}\Omega}{c^2\varepsilon_0 n_T} \int_0^\infty \frac{I_L}{n_0} d\omega, \quad (1)$$

$$\frac{\partial E_L}{\partial \zeta} = -\left(\frac{\gamma}{2}I_L^2 + iD_L\right)E_L + i\frac{\omega n_2}{c} \text{FT}\{E_r I_r\}, \quad (2)$$

where $E_T = E_T(\Omega, \zeta)$ and $E_L = E_L(\omega, \zeta)$ are the terahertz and laser fields, respectively, $\zeta = z - v_g t$ is the coordinate moving at the laser group velocity v_g , $\alpha = \alpha(\Omega)$ and $D_T = k(\Omega) - \Omega/v_g$ are the absorption (by bulk material and charge carriers) and dispersion at terahertz frequency Ω , d_{eff} is the effective terahertz nonlinear coefficient, n_0 and n_T are the refractive indices at laser and terahertz frequencies, and the term including $I_L = cn_0\varepsilon_0 E_L(\omega + \Omega, \zeta)E_L^*(\omega, \zeta)/2$ represents optical rectification by difference frequency mixing. The term including γ and $I_L^2 = c^2 n_0^2 \varepsilon_0^2 |E_L(\omega, \zeta)|^4/4$ indicates laser depletion by three-photon absorption, $D_L = k(\omega) - \omega/v_g$ is the dispersion at laser frequency ω , n_2 is the nonlinear index of refraction, E_r and I_r are the laser field and intensity in time at ζ , respectively, and FT denotes Fourier transformation. The last term in Eq. (2) describes laser self-phase modulation (SPM). Initially, the laser field is set to be a Gaussian pulse centered at 800 nm with a FWHM bandwidth of 50 nm. This yields an initial pulse width of 19 fs when no GDD was applied.

Figure 4(a) shows a simulated terahertz waveform captured 1 mm after exiting a 0.5-mm-thick LN when irradiated by a laser pulse with an initial GDD value of $-1,200$ fs². It shows two emerging terahertz pulses separated by 4.6 ps. The reason is that phase matching is not satisfied throughout the entire thickness of LN. Instead, nonvanishing terahertz arises from mostly the front and rear surfaces of LN within one coherence length, $l_c = \lambda_{\text{THz}}/[2(n_{\text{THz}} - n_g)] = 50$ μ m, from each surface. Here λ_{THz} is the wavelength at 1 THz, $n_{\text{THz}} = 5$ is the refractive index at 1 THz, and $n_g = 2.2$ is the group index at 800 nm. The first pulse at $t = 0$ ps is produced from near the rear surface of LN, whereas the second pulse at 4.6 ps is created from near the front end.

Figure 4(b) shows the radiation spectrum (black line) obtained via Fourier transformation of the waveform in (a). The spectrum agrees well with our measurement in Fig. 4. The fast modulations observed at <2 THz are due to interference between two temporally separated terahertz pulses. The spectrum of the first pulse (red line) is much broader and stronger than that of the second one (blue line). This is because absorption $\alpha(\Omega)$ in LN increases with frequency Ω , and the second pulse is affected more by this absorption. This also explains why the 0.5-mm-thick LN produces more terahertz radiation than the 1.0-mm one, as shown in Fig. 1. With a thinner LN, the laser pulse experiences less energy depletion and SPM until reaching

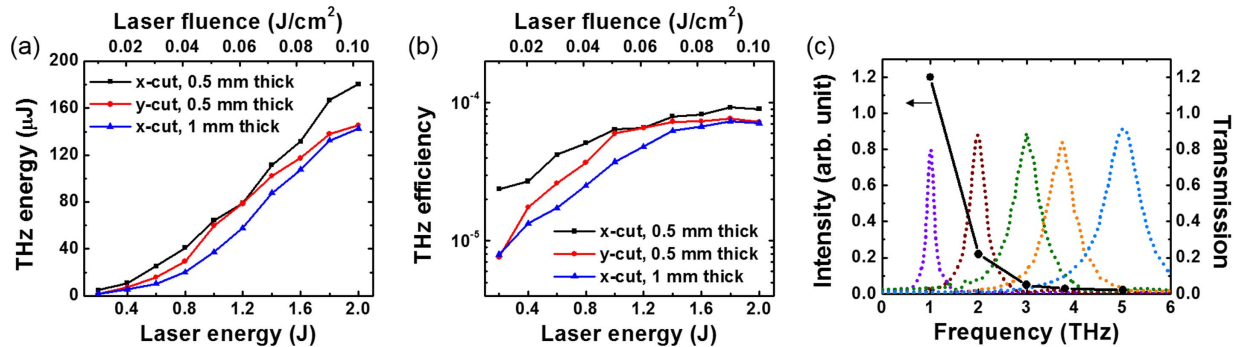


Fig. 3. (a) Terahertz output energy and (b) laser-to-terahertz conversion efficiency as function of laser energy or fluence. (c) Terahertz spectral power (scatters) measured with terahertz bandpass filters (1, 2, 3, 3.8, and 5 THz) when produced from the x-cut, 0.5-mm-thick LN at laser energy of 2 J with GDD of $-1,000$ fs². Coplotted are the spectral transmission curves of the filters (dotted lines).

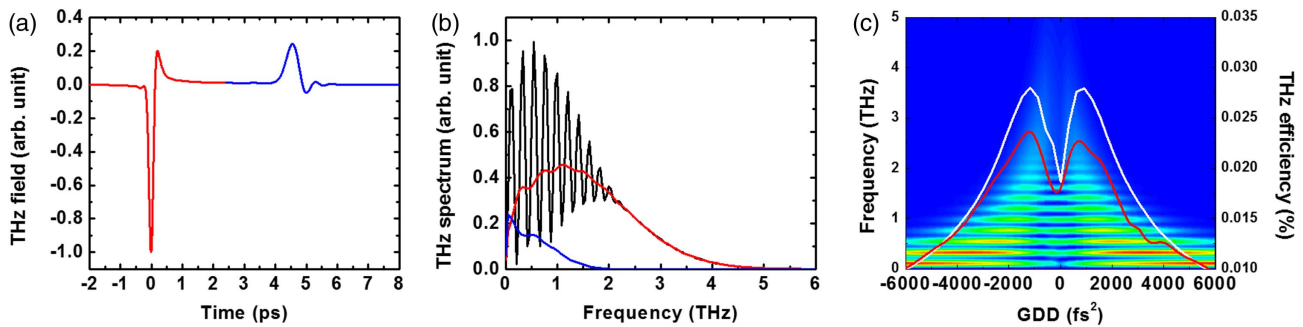


Fig. 4. (a) Simulated terahertz waveform produced from a 0.5-mm-thick LN when irradiated by a laser pulse with 2 J and GDD of $-1, 200 \text{ fs}^2$. (b) Simulated terahertz spectral power for the leading (red), lagging (blue), and combined (black) terahertz pulses in (a). (c) Simulated terahertz waveform (false color) and terahertz conversion efficiency obtained with zero (white line) and nonzero, real (red line) laser spectral phase obtained from Fig. 1(b).

the rear surface, and the terahertz emitted from the front side undergoes more absorption.

Figure 4(c) shows simulated terahertz spectral power as a function of laser input GDD. It well reproduces the suppressed terahertz emission when excited by short pulses. Through the simulation, we confirm that this is mainly caused by laser energy depletion via three-photon absorption, with little contribution from terahertz screening by charge carriers. The solid lines represent the overall terahertz conversion efficiency with all spectral power integrated. Those are obtained with a zero (white line) and nonzero, real (red line) laser spectral phase, respectively. With the measured phase taken into account, an asymmetric GDD dependence is clearly reproduced, consistent with the observation shown in Fig. 2. It also gives a maximum efficiency of 0.024%, not significantly different from our measured value (0.01%) given the fact that many coefficient values used in Eqs. (1) and (2) are unknown or not uniquely specified.

In conclusion, we have demonstrated scalable terahertz generation with Ti:sapphire laser energy up to 2 J using a 75-mm-diameter LN wafer. This provides terahertz conversion efficiencies approaching 10^{-4} in a simple setup. The scheme is easily upscalable by simply increasing the surface area of LN with more laser energy. For instance, a LN wafer with a 152-mm diameter, currently commercially available, can accommodate laser energy of 18.6 J at laser fluence of 0.1 J/cm^2 and produce output terahertz energy up to 1.7 mJ. Potentially, contact grating [20], contact tilted reflection [21], nonlinear echelon slab [22], or segmented tilted-pulse-front [23] schemes can be combined with a large LN to increase the coherence length for phase matching and thus produce even higher terahertz energy.

Funding. Air Force Office of Scientific Research (FA9550-16-1-0163); National Science Foundation (1351455); Gwangju Institute of Science and Technology; Institute for Basic Science (IBS-R012-D1); Office of Naval Research (N00014-17-1-2705).

REFERENCES

1. T. Kampfrath, K. Tanaka, and K. A. Nelson, *Nat. Photonics* **7**, 680 (2013).

2. H. A. Hafez, X. Chai, A. Ibrahim, S. Mondal, D. Férachou, X. Ropagnol, and T. Ozaki, *J. Opt.* **18**, 093004 (2016).
3. D. Nicoletti and A. Cavalleri, *Adv. Opt. Photon.* **8**, 401 (2016).
4. X. C. Zhang, A. Shkurinov, and Y. Zhang, *Nat. Photonics* **11**, 16 (2017).
5. F. Blanchard, L. Razzari, H.-C. Bandulet, G. Sharma, R. Morandotti, J.-C. Kieffer, T. Ozaki, M. Reid, H. F. Tiedje, H. K. Haugen, and F. A. Hegmann, *Opt. Express* **15**, 13212 (2007).
6. G. Polónyi, B. Monoszlai, G. Gäumann, E. J. Rohwer, G. Andriukaitis, T. Balciunas, A. Pugzlys, A. Baltuska, T. Feurer, J. Hebling, and J. A. Fülöp, *Opt. Express* **24**, 23872 (2016).
7. J. A. Fülöp, G. Polónyi, B. Monoszlai, G. Andriukaitis, T. Balciunas, A. Pugzlys, G. Arthur, A. Baltuska, and J. Hebling, *Optica* **3**, 1075 (2016).
8. A. Schneider, M. Neis, M. Stillhart, B. Ruiz, R. U. A. Khan, and P. Günter, *J. Opt. Soc. Am. B* **23**, 1822 (2006).
9. C. Vicario, A. V. Ovchinnikov, S. I. Ashitkov, M. B. Agranat, V. E. Fortov, and C. P. Hauri, *Opt. Lett.* **39**, 6632 (2014).
10. J. Hebling, A. G. Stepanov, G. Almási, B. Bartal, and J. Kuhl, *Appl. Phys. B* **78**, 593 (2004).
11. K.-L. Yeh, M. C. Hoffmann, J. Hebling, and K. A. Nelson, *Appl. Phys. Lett.* **90**, 171121 (2007).
12. A. G. Stepanov, S. Henin, Y. Petit, L. Bonacina, J. Kasparian, and J.-P. Wolf, *Appl. Phys. B* **115**, 293 (2014).
13. H. Hirori, A. Doi, F. Blanchard, and K. Tanaka, *Appl. Phys. Lett.* **98**, 091106 (2011).
14. X. Wu, S. Carbajo, K. Ravi, F. Ahr, G. Cirmi, Y. Zhou, O. D. Mücke, and F. X. Kärtner, *Opt. Lett.* **39**, 5403 (2014).
15. S.-C. Zhong, J. Li, Z.-H. Zhai, L.-G. Zhu, J. Li, P.-W. Zhou, J.-H. Zhao, and Z.-R. Li, *Opt. Express* **24**, 14828 (2016).
16. X.-J. Wu, J.-L. Ma, B.-L. Zhang, S.-S. Chai, Z.-J. Fang, C.-Y. Xia, D.-Y. Kong, J.-G. Wang, H. Liu, C.-Q. Zhu, X. Wang, C.-J. Ruan, and Y.-T. Li, *Opt. Express* **26**, 7107 (2018).
17. K. Ravi, W. R. Huang, S. Carbajo, X. Wu, and F. Kärtner, *Opt. Express* **22**, 20239 (2014).
18. C. Lombosi, G. Polónyi, M. Mechler, Z. Ollmann, J. Hebling, and J. A. Fülöp, *New J. Phys.* **17**, 083041 (2015).
19. Y. Yoo, D. Jang, M. Kimbrue, and K. Kim, in *Frontiers in Optics/Laser Science*, OSA Technical Digest (Optical Society of America, 2018), paper JW3A.52.
20. L. Pálfalvi, J. A. Fülöp, G. Almási, and J. Hebling, *Appl. Phys. Lett.* **92**, 171107 (2008).
21. Y. J. Yoo, "High-field THz generation and beam characterization with laser based intense THz sources," Ph. D. dissertation (University of Maryland, 2018).
22. P. S. Nugraha, G. Krizsán, C. Lombosi, L. Pálfalvi, G. Tóth, G. Almási, J. A. Fülöp, and J. Hebling, *Opt. Lett.* **44**, 1023 (2019).
23. G. Tóth, L. Pálfalvi, J. A. Fülöp, G. Krizsán, N. H. Matlís, G. Almási, and J. Hebling, *Opt. Express* **27**, 7762 (2019).